

# OPENPROS: A Large-Scale Dataset for Limited View Prostate Ultrasound Computed Tomography

Hanchen Wang<sup>1,\*</sup>, Yixuan Wu<sup>2,\*</sup>, Yinan Feng<sup>1</sup>, Peng Jin<sup>3</sup>, Shihang Feng<sup>1</sup>,  
Yiming Mao<sup>1</sup>, James Wiskin<sup>4</sup>, Baris Turkbey<sup>5</sup>, Peter A. Pinto<sup>5</sup>, Bradford J. Wood<sup>5</sup>,  
Songting Luo<sup>6</sup>, Yinpeng Chen<sup>7,†</sup>, Emad Boctor<sup>2</sup>, and Youzuo Lin<sup>1</sup>

<sup>1</sup>University of North Carolina at Chapel Hill, <sup>2</sup>Johns Hopkins University,

<sup>3</sup>The Pennsylvania State University, <sup>4</sup>QT Imaging, Inc.,

<sup>5</sup>National Institutes of Health, <sup>6</sup>Iowa State University, <sup>7</sup>Google DeepMind

## Abstract

Prostate cancer is one of the most common and lethal cancers among men, making its early detection critically important. Although ultrasound imaging offers greater accessibility and cost-effectiveness compared to MRI, traditional transrectal ultrasound (TRUS) methods suffer from low sensitivity, especially in detecting anteriorly located tumors. Ultrasound computed tomography (USCT) provides quantitative tissue characterization, but its clinical implementation faces significant challenges, particularly under anatomically constrained limited-angle acquisition conditions specific to prostate imaging. To address these unmet needs, we introduce OPENPROS, the first large-scale benchmark dataset explicitly developed for limited-view prostate USCT. Our dataset includes over 280,000 paired samples of realistic 2D speed-of-sound (SOS) phantoms and corresponding ultrasound full-waveform data, generated from anatomically accurate 3D digital prostate models derived from real clinical MRI/CT scans and ex vivo ultrasound measurements, annotated by medical experts. Simulations are conducted under clinically realistic configurations using advanced finite-difference time-domain (FDTD) and Runge-Kutta acoustic wave solvers, both provided as open-source components. Through comprehensive baseline experiments, we demonstrate that state-of-the-art deep learning methods surpass traditional physics-based approaches in both inference efficiency and reconstruction accuracy. Nevertheless, current deep learning models still fall short of delivering clinically acceptable high-resolution images with sufficient accuracy. By publicly releasing OPENPROS, we aim to encourage the development of advanced machine learning algorithms capable of bridging this performance gap and producing clinically usable, high-resolution, and highly accurate prostate ultrasound images. The dataset is publicly accessible at <https://open-pros.github.io/>.

## 1 Introduction

Prostate cancer is the second most common malignancy among men and is one of the leading causes of cancer-related deaths worldwide, and every eight men suffers from it [19, 23]. Since the 5-year survival rate for prostate cancer patients significantly drops from nearly 100% to approximately 34% once the disease progresses from localized or regional stages to distant metastases [12], early

\*Equal contribution

†Advisory capacity only

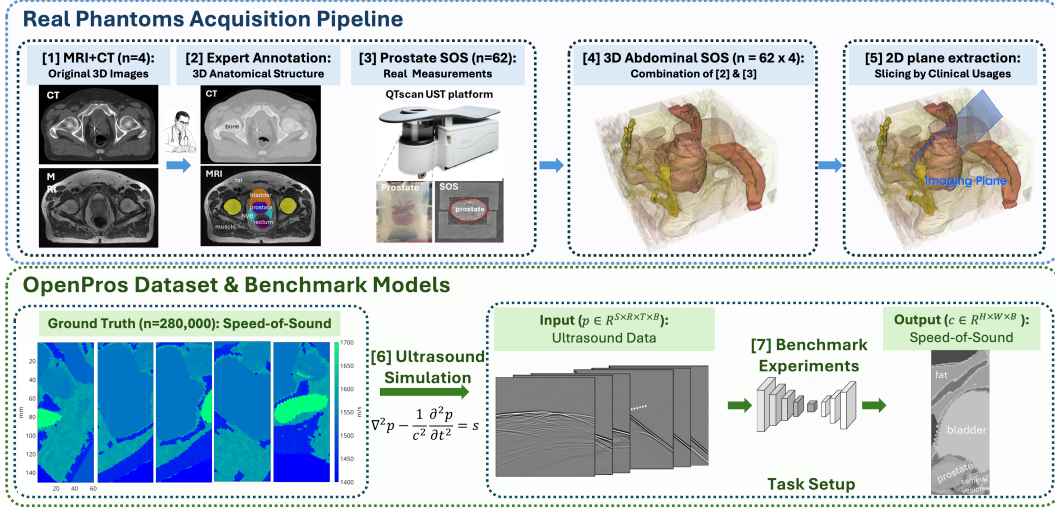


Figure 1: **OPENPROS dataset creation and benchmarking pipeline.** Top panel: Starting from clinical MRI and CT scans, we employ expert annotations to generate detailed 3D anatomical segmentations. We then incorporate real ultrasound speed-of-sound (SOS) measurements from ex vivo prostate samples acquired using the QTscan platform. These are integrated into comprehensive 3D abdominal SOS models. Clinically relevant 2D slices are subsequently extracted from these models to simulate limited-angle ultrasound tomography scenarios. Bottom panel: The extracted 2D SOS maps form the ground truth for ultrasound simulations governed by the acoustic wave equation. The resulting simulated ultrasound data are organized into the OPENPROS dataset. We utilize these data to train and benchmark physics-based and deep-learning inversion methods, facilitating the evaluation and development of rapid, clinically relevant SOS reconstruction methods under challenging limited-angle conditions.

detection of aggressive prostate cancer is of vital importance. Medical imaging plays an essential role in this early detection. Among the available imaging modalities, multiparametric MRI (mpMRI) is currently recognized as the most advanced and accurate imaging tool for detecting and localizing clinically significant prostate cancer. However, the high cost and limited accessibility of mpMRI restrict its widespread adoption, particularly in rural or low-resource settings [7, 13].

In contrast, ultrasound imaging is widely accessible, cost-effective, and capable of real-time imaging. Prostate ultrasound is typically performed transrectally, producing B-mode (brightness-mode) images. Although transrectal ultrasound (TRUS) is the clinical standard for routine prostate evaluations and biopsy guidance, it has a sensitivity of only 30%–50% for detecting clinically significant tumors and a specificity of 70%–80% [4, 5]. Studies have further shown that tumors located in the anterior or apical prostate regions are often undetectable with TRUS due to poor soft-tissue contrast and restricted acoustic windows, and TRUS cannot reliably distinguish malignant lesions from benign conditions such as chronic prostatitis [16].

Ultrasound computed tomography (USCT) has emerged as a promising alternative, reconstructing quantitative tissue parameters such as speed-of-sound (SOS) and acoustic attenuation, which serve as potential biomarkers for malignancy [28, 26]. However, the anatomical constraints of prostate imaging inherently limit the acquisition aperture, creating a challenging scenario referred to as the *limited-angle condition*. Unlike idealized imaging setups where transducers surround the entire imaging domain, prostate imaging is anatomically restricted to transrectal and transabdominal placements, resulting in sparse and angularly limited data. Traditional physics-based methods typically struggle under these conditions, demonstrating slow convergence, severe ill-posedness, and significant reconstruction artifacts [25, 10]. Developing robust USCT algorithms capable of accurately handling limited-angle data is thus critically needed for clinical prostate imaging.

Furthermore, clinical translation of prostate USCT faces considerable barriers due to the complexity and specialization of current imaging systems. To date, only two USCT systems (SoftVue and QTscan) have received U.S. FDA approval, and both systems focus exclusively on full-angle breast imaging with custom hardware setups unsuited for prostate applications [21, 15]. These existing systems operate at relatively low frequencies, rely on patient positioning incompatible with prostate imaging, and require hours for reconstruction. Thus, there is an urgent need for efficient, generalizable, and clinically adaptable prostate-specific USCT platforms. Crucially, this advancement depends on the availability of realistic, anatomically precise digital phantoms and datasets, which are currently lacking in the field [10, 1].

Additionally, prostate imaging complexity is increased by high tissue heterogeneity and proximity to multiple adjacent organs and bony pelvic structures, invalidating simplified fluid medium assumptions typically used in breast imaging. These factors severely compromise USCT image reconstruction quality, further emphasizing the necessity of specialized prostate-specific datasets.

Recent advances in deep learning, particularly convolutional neural networks (CNNs), have shown potential for overcoming these limitations by learning complex mappings directly from ultrasound data to high-resolution SOS maps [6, 11]. Data-driven approaches bypass computational bottlenecks encountered by iterative solvers and demonstrate the ability to reconstruct detailed tissue properties even under sparse and noisy acquisition conditions. Instead of hours to days of image reconstruction using physics-based methods and the requirement of expert reading as a follow-up, the relatively short inference time and the automatic analysis enable faster and easier diagnosis for better patient experience. Furthermore, transformer-based architectures have recently demonstrated remarkable performance in medical imaging by effectively modeling long-range spatial dependencies, a feature particularly beneficial for ultrasound tomography due to the extensive spatial interaction of acoustic waves.

Despite these advancements, progress has been significantly hampered by the lack of large-scale, high-fidelity datasets supporting the development, evaluation, and reproducibility of innovative reconstruction algorithms. Existing USCT datasets are typically for breast imaging, which are either synthesized in simulation or derived from real phantoms. Related datasets are listed in Table 1. They exhibit diversities and reflect anatomical realism to a good extent but not the best. There are also anatomical datasets for the male pelvic region but not for USCT purposes. The commercial anatomy softwares such as Zygote Body and Complete Anatomy provide different pricing options for viewing and downloading, but they generally lack anatomical varieties. Last but not least, no publicly available dataset adequately addresses the unique challenges posed by limited-view prostate ultrasound computed tomography and the existence of bones in the imaging view while simultaneously providing realistic wave propagation modeling and comprehensive full-waveform data.

Table 1: **Comparison between our OPENPROS and other existing datasets for the male pelvic region or for medical ultrasound computed tomography.** The symbols  $\checkmark$ ,  $\times$ , and NA indicate that the dataset contains, does not contain, or is not applicable to the corresponding feature, respectively.

Dataset	Prostate	Acoustic parameters	Actual anatomy	Tissue heterogeneity	Bones	Limited angle	Public	Free access
<b>OPENPROS (ours)</b>	$\checkmark$	$\checkmark$	$\checkmark$	$\checkmark$	$\checkmark$	$\checkmark$	$\checkmark$	$\checkmark$
Li <i>et al.</i> [14]	$\times$	$\checkmark$	$\times$	$\checkmark$	$\times$	$\times$	$\checkmark$	$\checkmark$
Ruiter <i>et al.</i> [20]	$\times$	$\checkmark$	$\times$	$\checkmark$	$\times$	$\times$	$\checkmark$	$\checkmark$
OpenWaves [31]	$\times$	$\checkmark$	$\times$	$\checkmark$	$\times$	$\times$	$\checkmark$	$\checkmark$
Segars <i>et al.</i> [22]	$\checkmark$	$\times$	$\checkmark$	NA	$\checkmark$	NA	$\checkmark$	$\times$
The visible human project [2]	$\checkmark$	$\times$	$\checkmark$	NA	$\checkmark$	NA	$\checkmark$	$\checkmark$
Zygote Body	$\checkmark$	$\times$	$\checkmark$	NA	$\checkmark$	NA	$\checkmark$	$\checkmark$
Complete Anatomy	$\checkmark$	$\times$	$\checkmark$	NA	$\checkmark$	NA	$\checkmark$	$\times$

Motivated by these challenges and inspired by the success of OPENFWI [8] and  $\mathbf{E}^{FWI}$  [9] datasets, we introduce OPENPROS, the first large-scale dataset specifically designed for limited-angle prostate USCT scenarios. A schematic illustration of the overall pipelines of OPENPROS is shown in Figure 1. Our dataset comprises over 280,000 paired 2D SOS phantoms and ultrasound full-waveform data derived from anatomically realistic 3D prostate models generated from clinical MRI/CT scans and ex vivo ultrasound measurements, annotated meticulously by clinical experts. OPENPROS serves as a critical benchmark facilitating advances in computational efficiency, limited-angle reconstruction accuracy, rapid clinical adaptability, and comprehensive method comparisons across various imaging conditions, including ray-based, single scattering, high-frequency, and limited-angle scenarios.

In summary, our contributions to the community include:

1. **Large-scale, anatomically realistic benchmark dataset:** The first comprehensive prostate USCT dataset, derived from clinical MRI/CT scans and detailed expert annotations, designed explicitly to address limited-angle imaging conditions.
2. **High-fidelity, publicly available simulation tools:** Advanced finite-difference time-domain (FDTD) and Runge-Kutta implicit iterative acoustic solvers, openly accessible alongside our dataset to facilitate reproducibility and method development.
3. **Comprehensive benchmarking of inversion methods:** Thorough evaluation of physics-based and state-of-the-art deep learning methods under realistic limited-angle conditions, establishing clear performance baselines and guiding future algorithmic improvements.

The remainder of this paper is structured as follows: In Section 2, we overview the fundamentals of USCT and our task setup. Section 3 details our dataset construction. Section 4 describes benchmarking experiments. In Section 6, we discuss dataset strengths, limitations, and future research directions. Finally, we conclude in Section 7 by summarizing our key contributions and the broader implications of OPENPROS.

## 2 Ultrasound Computed Tomography and Forward Modeling

In the context of USCT, the forward problem involves simulating acoustic wave propagation through soft tissues, which is governed by the acoustic wave equation. Assuming an isotropic medium with constant density, the forward modeling equation is given by:

$$\nabla^2 p - \frac{1}{c^2} \frac{\partial^2 p}{\partial t^2} = s, \quad (1)$$

where  $\nabla^2 = \frac{\partial^2}{\partial x^2} + \frac{\partial^2}{\partial y^2}$  in 2D,  $c(x, y)$  denotes the spatially varying SOS map,  $p(x, y, t)$  is the acoustic pressure field, and  $s(x, y, t)$  represents the ultrasound source. In our simulations, the source  $s$  is prescribed as a controlled ultrasound excitation. Clinically, the primary goal of ultrasound tomography is to reconstruct spatially varying SOS maps from recorded pressure fields, enabling accurate tissue characterization and anomaly detection, such as identifying tumors or lesions.

The forward modeling of ultrasound propagation thus entails computing the pressure field  $p$  from a given SOS distribution  $c$ , represented by the highly nonlinear mapping  $p = f(c)$ , where  $f(\cdot)$  encapsulates the complex wave propagation phenomena defined by Equation (1). In practice, the recorded ultrasound signals form a 4-dimensional tensor  $p \in \mathbb{R}^{S \times R \times T \times B}$ , where  $S$  is the number of sources,  $R$  is the number of receivers,  $T$  represents the number of time steps, and  $B$  denotes the batch dimension. Specifically, in our simulated prostate dataset, we set  $S = 20$ ,  $R = 322$ , and  $T = 1000$ . The output SOS maps to be reconstructed are represented as 3-dimensional tensors  $c \in \mathbb{R}^{H \times W \times B}$ , where  $H$  and  $W$  represent the spatial height and width dimensions, respectively. In our specific configuration, each SOS map has a spatial resolution of  $401 \times 161$  grid points.

Data-driven USCT leverages neural networks to directly approximate the inverse mapping  $c = f^{-1}(p)$ , as demonstrated in recent studies [30]. Thus, the specific task addressed in this paper is the supervised learning problem, formulated as  $\min_{\theta} \mathbb{E}_p, c [\mathcal{L}(c, \hat{c})]$ , where  $\hat{c} = f_{\theta}^{-1}(p)$ . Here,  $f_{\theta}^{-1}$  represents a deep neural network parameterized by  $\theta$ , trained on pairs of simulated ultrasound signals  $p$  and corresponding ground-truth SOS maps  $c$ . The training objective  $\mathcal{L}$  typically incorporates quantitative metrics such as Mean Absolute Error (MAE), Root Mean Squared Error (RMSE), Structural Similarity Index Measure (SSIM) and Pearson Correlation Coefficient (PCC).

## 3 OPENPROS Dataset

OPENPROS is the *first* large-scale benchmark dataset explicitly designed to facilitate research in limited-angle prostate ultrasound computed tomography (USCT). It contains anatomically realistic 2D speed-of-sound phantoms, organ segmentation labels, and corresponding simulated ultrasound waveforms derived from detailed 3D digital prostate models. The patient level anatomy ID is named as 3\_01, 3\_02, 3\_03 and 3\_04. The prostate level anatomy ID is named as the date of acquisition (in total 62 prostates). Detailed naming strategy can be found in the Appendix C.

In the following subsections, we first show the basic statistics of our dataset and highlight the related domain interests. We then describe the design strategies of 3D/2D prostate phantoms which maximize the fidelity. At the end, we discuss the ultrasound data simulation setups.

### 3.1 Dataset Statistics

OPENPROS consists of 280,000 paired examples of 2D SOS phantoms and ultrasound data, systematically derived from realistic 3D digital models. The essential characteristics and data dimensions are summarized in Table 2.

OPENPROS supports various critical research topics, including:



Table 2: **Dataset summary for the OpenPros USCT dataset.** SOS maps are formatted as (sample  $\times$  channel (#physical params, SOS here)  $\times$  depth (vertical)  $\times$  width (horizontal)); ultrasound data as (sample  $\times$  channel (#sources)  $\times$  time  $\times$  #receivers).

Dataset	Size	#Train / #Validation / #Test	Ultrasound Data Shape	SOS Map Shape
OpenPros	6.8 TB	224K / 28K / 28K	$1140 \times 40 \times 1000 \times 161$	$1140 \times 1 \times 401 \times 161$

**Tissue Interfaces:** Clearly defined interfaces among prostate, bladder, and surrounding tissues, essential for organ boundary delineation and accurate pathology differentiation. Segmentation labels enhance precision in evaluating inversion algorithms.

**Lesion Characterization:** Realistically modeled synthetic lesions (e.g., tumors) introduce SOS discontinuities, challenging algorithms in lesion detection and characterization, critical for diagnostic accuracy.

**Clinical Variability and Realistic Imaging Conditions:** Systematic slicing of high-resolution 3D digital models captures realistic anatomical variability, with advanced finite-difference time-domain (FDTD) simulations reflecting clinical imaging conditions, including limited aperture, acoustic noise, and tissue heterogeneity.

**Anatomy-Aware Inversion:** Integrated segmentation masks guide targeted inversion studies, emphasizing reconstruction accuracy in clinically significant regions, thus promoting anatomically detailed reconstruction assessments.

Our sophisticated data generation pipeline, encompassing digital phantom modeling, detailed anatomical labeling, and precise acoustic simulations, significantly enhances the clinical relevance and diversity of the dataset.

### 3.2 3D Prostate Phantom Design

It is important to note that the 3D digital phantoms were derived from human CT/MRI [17] and USCT scans of ex vivo prostate specimens [18, 27, 26]. Major organs were annotated by experts using T2-weighted MRI, fat was segmented from T1-weighted MRI, bones were segmented from X-ray CT, and the speed of sound and attenuation of ex vivo prostate samples were measured using a QT scanner (QT Imaging Inc., Novato, California, USA). Speed of sound of other organs were acquired from ITIS foundation tissue database [3]. To best mimic the tissue heterogeneity, we employed Gaussian distributions with given mean values and standard deviations from the tissue database to assign speed of sound in different tissue types. These derivations from human data reduces the reliance on synthetic simulation and maximizes the fidelity of the dataset, especially in the prostate area. Additional details on phantom construction, applications, and open access availability can be found in [29]. The 3D abdominal anatomical structure and the ultrasound probe placement sketch can be found in Figure 2(a) and the illustration of 3D phantom can be found in Figure 2(b).

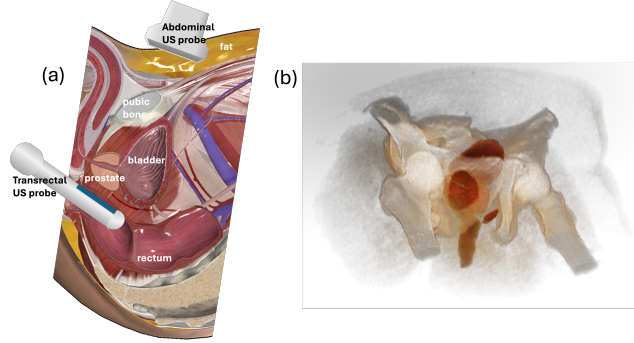


Figure 2: **(a) Anatomical structure and probe placement.** Two probes-abdominal (on the body surface) and transrectal (in the rectum)-are used in our simulation. Image courtesy of Complete Anatomy. **(b) 3D digital SOS phantom.** SOS distribution in the anatomically realistic prostate model.

### 3.3 2D Prostate Phantom Extraction

We generate 2D speed-of-sound phantoms by slicing our anatomically realistic 3D prostate volumes under clinically realistic probe configurations. For each phantom, we place one transrectal probe in the rectum and one abdominal probe on the body surface, then sample cross-sections across a range of rotations ( $\pm 45^\circ$ ) and small random perturbations. This process yields 280 K paired 2D SOS maps and corresponding ultrasound waveforms that faithfully capture patient-specific anatomy and limited-angle acquisition variability.

More detailed 2D phantom extraction strategy can be found in Appendix B

### 3.4 Ultrasound Data Simulation

We simulate ultrasound wave propagation using a finite-difference time-domain (FDTD) solver based on the 2D acoustic wave equation discussed above. The numerical scheme adopts fourth-order accuracy in space and second-order accuracy in time, offering a reliable trade-off between numerical precision and computational efficiency. This configuration is particularly well-suited for capturing fine-grained wave interactions in heterogeneous prostate tissue environments.

Each simulation is conducted under two acquisition configurations, placing sources and receivers along the top and bottom boundaries of the computational grid. A total of 20 sources (10 at the top and 10 at the bottom, shown as yellow stars in Figure 3) are uniformly distributed along each boundary. For every source, 322 receivers (shown as red dots in Figure 3) are placed across the entire lateral extent of the domain, enabling comprehensive capture of the scattered wavefield. A Ricker wavelet with a 1 MHz peak frequency serves as the excitation pulse, consistent with clinical transducer characteristics. The wavefield is recorded over 1,000 time steps at a sampling interval of  $\Delta t = 1 \times 10^{-7}$  seconds, covering a total duration of 100  $\mu s$ . To suppress artificial reflections, 120 grid points of absorbing boundary condition (ABC) are applied to each boundary. Two examples of our simulations and the corresponding SOS maps are shown in Figure 3.

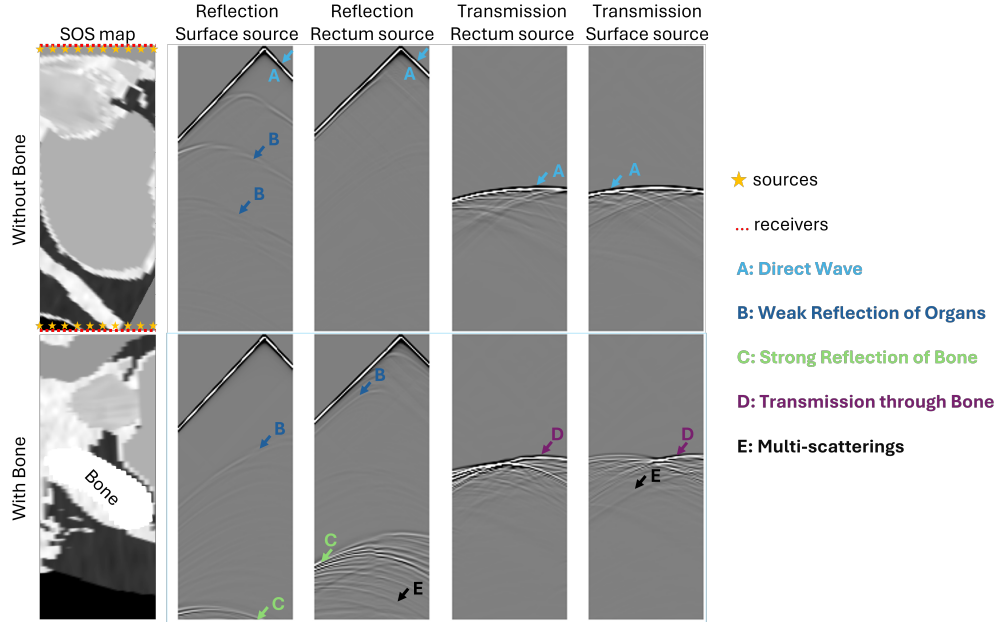


Figure 3: **Examples of simulated ultrasound data and phantoms:** without (top) and with (bottom) bone in the phantoms. We show two example channels of reflections and transmissions with sources (yellow stars) and receivers (red dots) on the two probes. Our PDE solvers can simulate complex and realistic ultrasound wave phenomena, such like transmissions, reflections, direct waves and multi-scatterings.

The spatial discretization of the domain uses a grid spacing of 0.375 mm, resulting in a field of view of approximately 60 mm in depth and 150 mm in width. This configuration mirrors the anatomical scale of the prostate and its surrounding structures. A summary of the physical simulation parameters and the physical meaning of the dimension is shown in Table 3.

Table 3: **Physical Meaning of the Prostate USCT Dataset**

Dataset	Grid Spacing	SOS Map Spatial Size	Source Spacing	Source Line Length	Receiver Spacing	Receiver Line Length	Time Spacing	Recorded Time
OpenPros	0.375 mm	60 mm $\times$ 150 mm	37.5 mm	60 mm	3.75 mm	60 mm	$1 \times 10^{-7}$ s	100 $\mu s$

Importantly, the simulated ultrasound data for each sample contains 40 distinct channels, organized to reflect practical probe configurations: Channels (0–9) Source on body surface, receiver on body

surface; (10–19) source on body surface, receiver in rectum; (20–29) source in rectum, receiver in rectum; and (30–39) source in rectum, receiver on body surface. This setup emulates both conventional transabdominal and transrectal imaging pathways, enabling detailed studies of transmission and reflection across diverse acoustic paths.

#### 4 OPENPROS Benchmarks

OPENPROS lets us systematically investigate three core questions under limited-angle prostate USCT: (1) **Inference efficiency**, (2) **Reconstruction accuracy**, and (3) **OOD generalization**.

Table 4: **Quantitative results** of benchmarking methods on the prostate USCT dataset.

Method	MAE↓	RMSE↓	SSIM↑	PCC↑
InversionNet	<b>0.0089</b>	<b>0.0433</b>	<b>0.9845</b>	<b>0.9798</b>
ViT-Inversion	0.0123	0.0566	0.9774	0.9728

**Methods & Metrics** We compare two physics-based baselines-Delay-and-Sum Beamforming and multi-stage physics-based USCT inversion-against two data-driven models: InversionNet, and ViT-Inversion. Performance is measured with four metrics: mean absolute error (MAE) and root-mean-square error (RMSE) for numerical fidelity, plus SSIM and Pearson correlation (PCC) for perceptual and structural similarity. All models are trained and evaluated under identical settings on NVIDIA H100 GPUs.

##### 4.1 Benchmark Methods for Prostate USCT

**Beamforming**, a classical ultrasound imaging method, reconstructs images by aligning and summing received ultrasound echoes according to assumed sound speeds and propagation paths. In this baseline, beamforming serves as a fast, widely-adopted approach for generating initial ultrasound images, highlighting the inherent limitations under restricted-view conditions.

**Physics-based USCT** is performed in a three-stage multi-frequency framework. Starting from a smoothed initial SOS model, we first invert low-frequency data, then mid-frequency data, and finally full-band data. At each stage, synthetic waveforms are generated via our forward operator and compared to observed data; the SOS model is updated by minimizing the waveform misfit.

**InversionNet** [30] proposed a fully-convolutional network to model the seismic inversion process. With the encoder and the decoder, the network was trained in a supervised scheme by taking 2D (time  $\times$  # of receivers) seismic data from multiple sources as the input and predicting 2D (depth  $\times$  length) velocity maps as the output.

**ViT-Inversion**: A Vision Transformer that partitions the 4D waveform tensor  $[B, S, T, R]$  into spatio-temporal patches, embeds them into tokens, and applies multi-head self-attention to capture long-range wave interactions. A lightweight upsampling CNN refines the patch-wise outputs into full-resolution SOS maps.

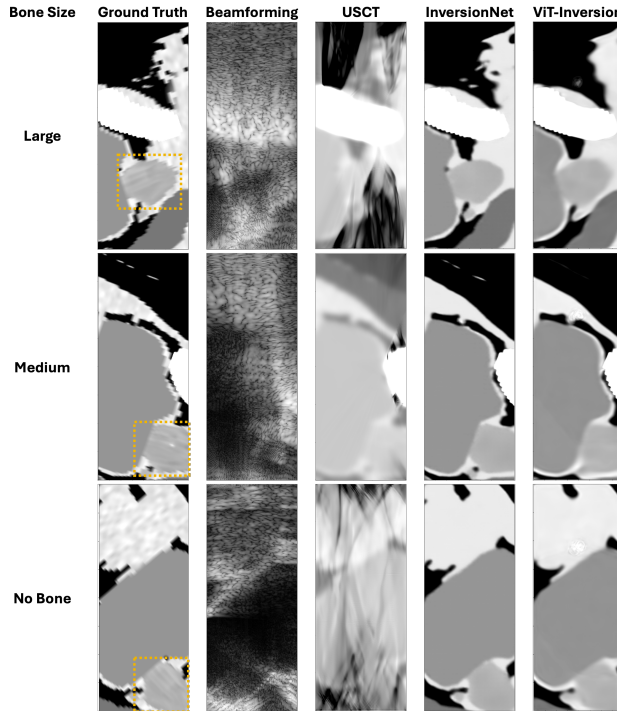


Figure 4: **Benchmark results for limited-angle prostate USCT.** Each column shows a different inversion method on the same phantom: (col 1) ground-truth SOS map; (col 2) Delay-and-Sum beamforming; (col 3) physics-based USCT; (col 4) InversionNet; (col 5) ViT-Inversion. Rows correspond to three representative prostate slices illustrating challenging (top), moderate (middle), and simple (bottom) anatomical scenarios. Zoom-in figures of the prostate region (orange squares) are shown in Figure 5.

(Training details in App. E.)

## 4.2 Result Analysis

**Quantitative Results** Table 4 reports mean absolute error (MAE), root mean squared error (RMSE), structural similarity index (SSIM), and Pearson correlation coefficient (PCC) for our two learned baselines. Traditional physics-based USCT (not shown) achieves an RMSE around 0.16 and SSIM  $\sim 0.90$ , roughly halving the error of simple beamforming but still leaving significant room for improvement. In contrast, InversionNet reduces RMSE to 0.0433-nearly a fourfold improvement over physics-based inversion-and attains the highest MAE (0.0089), SSIM (0.9845), and PCC (0.9798). ViT-Inversion also outperforms the physics-based approach, cutting RMSE in half (0.0566) and achieving an SSIM of 0.9774.

### Qualitative Observations

Figure 4 presents three representative prostate slices under challenging (top), moderate (middle), and simple (bottom) anatomical conditions. Delay-and-Sum beamforming yields noisy, low-contrast images incapable of resolving detailed prostate structures. Physics-based USCT significantly reduces these artifacts and better recovers the general gland shape but produces overly blurred images lacking fine anatomical details. Machine learning-based methods, including InversionNet and ViT-Inversion, markedly outperform physics-based USCT in reconstructing the global anatomical structure and boundaries. However, the zoom-in prostate images shown in Figure 5 illustrate that despite better overall shape reconstruction, these learned methods still cannot accurately resolve fine structures within the prostate. The internal prostate structures remain smoothed, and small lesions or detailed boundaries are not distinctly reconstructed, indicating significant room for improvement in imaging resolution and accuracy.

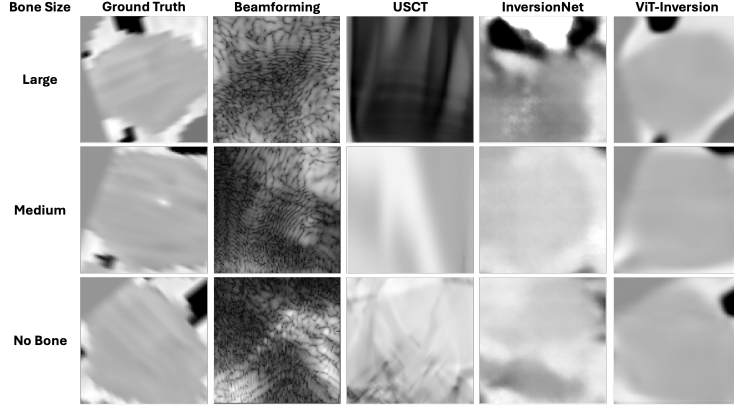


Figure 5: **Zoom-in comparison of prostate regions.** Enlarged views (orange squares in Figure 4) showing detailed reconstruction quality within the prostate region across baseline methods: (col 1) Ground truth; (col 2) Delay-and-Sum beamforming; (col 3) physics-based USCT; (col 4) InversionNet; (col 5) ViT-Inversion. Each row corresponds to the same anatomical scenario as in Figure 4. Note that although the learned methods recover general anatomical shapes more clearly, the fine internal structures and boundaries remain poorly resolved.

**Inference Efficiency Comparison** In addition to superior accuracy, data-driven methods offer remarkable computational efficiency suitable for real-time imaging applications, as summarized in Table 7 (see appendix). Traditional physics-based inversions, such as beamforming and multi-stage USCT, incur significant computational overheads, requiring approximately 4 hours and 24 hours per sample, respectively. In sharp contrast, the data-driven approaches achieve near-instantaneous reconstructions: InversionNet requires only 4.9 milliseconds per sample, while ViT-Inversion completes inference in roughly 8.9 milliseconds due to its transformer architecture. This stark difference highlights the practical feasibility and potential clinical value of learned models in enabling rapid, real-time prostate imaging.

## 5 Ablation Study

To assess how well our models generalize to truly unseen anatomies, we conducted three out-of-distribution tests using data splits that reflect realistic clinical scenarios: **(1) Patient-Level Generalization:** Train on patients 3\_01, 3\_02, 3\_03, test on an entirely unseen patient 3\_04. **(2) Leave-One-Prostate-Out:** Train on 60 prostates from all four patients except two held-out prostate (i.e. 2022-06-06 & 2022-06-09), test on those withheld prostates. **(3) Combined Generaliza-**

**tion:** Train on 60 prostates drawn only from patients 3\_01–3\_03, test on both remaining prostates of patient 3\_04.

Table 5 summarizes MAE, RMSE, SSIM, and PCC for InversionNet and ViT-Inversion under each scenario. In the *patient-level generalization* test, all methods suffer substantial performance degradation. InversionNet’s MAE increases from 0.0089 (within-distribution) to 0.0653 and its RMSE from 0.0433 to 0.2465, while SSIM falls to 0.9111. ViT-Inversion experiences a similar drop, with MAE rising to 0.0802, RMSE to 0.2898, and SSIM to 0.9055. This indicates that entirely novel patient anatomies pose a significant challenge for learned inversion models.

By contrast, the *leave-one-prostate-out* test shows only minimal accuracy loss. InversionNet maintains MAE=0.0070, RMSE=0.0291, and SSIM=0.9886, nearly matching in-distribution performance. ViT-Inversion also remains strong with MAE=0.0100, RMSE=0.0424, and SSIM=0.9823. These results suggest that intra-patient anatomical variability is comparatively easier for the networks to handle.

The most demanding *combined OOD* scenario amplifies the accuracy drop. InversionNet’s SSIM settles at 0.9137 (MAE=0.0624, RMSE=0.2370), and ViT-Inversion achieves SSIM=0.8972 (MAE=0.0862, RMSE=0.3045). Although InversionNet retains slightly higher fidelity under these extreme conditions, neither method reaches within-distribution levels, underscoring that truly patient-agnostic reconstruction remains an open challenge.

Overall, these ablations demonstrate that while machine learning based methods significantly outperform physics-based USCT under matched conditions, their ability to generalize to entirely unseen anatomies is still limited.

Table 5: **Generalization Test Results.** Evaluation of inversion methods on unseen prostate anatomies.

Scenario	Method	MAE↓	RMSE↓	SSIM↑	PCC↑
Patient-level	InversionNet	0.0653	0.2465	0.9111	0.6574
	ViT-Inversion	0.0802	0.2898	0.9055	0.6098
Leave-one-prostate	InversionNet	0.0070	0.0291	0.9886	0.9891
	ViT-Inversion	0.0100	0.0424	0.9823	0.9852
Combined OOD	InversionNet	0.0624	0.2370	0.9137	0.6753
	ViT-Inversion	0.0862	0.3045	0.8972	0.5774

## 6 Discussion

Our OPENPROS dataset offers an unprecedented resource for developing limited-angle prostate USCT algorithms. With over 280,000 paired SOS phantoms and ultrasound simulations derived from clinical data, it realistically captures tissue heterogeneity and anatomical constraints of prostate imaging. Our open-source FDTD and Runge-Kutta solvers ensure transparent benchmarking and reproducibility.

However, the dataset currently includes a limited number of patient anatomies, potentially underrepresenting certain anatomical variations. Additionally, we simulate only SOS distributions, omitting other critical acoustic parameters like attenuation and density. Our 2D simulations do not account for three-dimensional propagation and out-of-plane scattering, simplifying some real-world conditions.

Future work will expand the patient dataset, introduce multiparametric acoustic maps, and extend simulations to three dimensions. Incorporating clinically relevant pathologies and carefully designed out-of-distribution scenarios will further enhance the robustness and clinical applicability of future USCT solutions.

## 7 Conclusion

In this work, we have introduced OPENPROS, the first comprehensive, large-scale benchmark dataset specifically designed for limited-angle prostate ultrasound computed tomography. With over 280,000 expertly annotated 2D speed-of-sound phantoms paired with high-fidelity simulated ultrasound data, OPENPROS facilitates efficient benchmarking of both physics-based and advanced deep learning reconstruction algorithms. Our baseline experiments clearly demonstrate that deep learning approaches significantly outperform conventional physics-based methods in terms of inference speed and image quality. However, critical challenges remain, notably in resolving fine anatomical details within the prostate and achieving robust generalization across unseen anatomies. By making OPENPROS publicly available, we encourage the research community to leverage and expand this foundational resource, ultimately advancing toward clinically viable, high-resolution prostate imaging solutions.

## References

- [1] Fereshteh Aalamifar, Rishabh Khurana, Alexis Cheng, Xiaoyu Guo, Iulian Iordachita, and Emad M Boctor. Enabling technologies for robot assisted ultrasound tomography. *The International Journal of Medical Robotics and Computer Assisted Surgery*, 13(1):e1746, 2017.
- [2] Michael J Ackerman. The visible human project. *Proceedings of the IEEE*, 86(3):504–511, 1998.
- [3] C Baumgartner, PA Hasgall, F Di Gennaro, E Neufeld, B Lloyd, MC Gosselin, D Payne, A Klingeböck, and N Kuster. It’s database for thermal and electromagnetic parameters of biological tissues. *IT’IS Found., Zurich, Switzerland, Tech. Rep*, 4, 2024.
- [4] PMM Beemsterboer, R Kranse, HJ De Koning, JDF Habbema, and FH Schröder. Changing role of 3 screening modalities in the european randomized study of screening for prostate cancer (rotterdam). *International journal of cancer*, 84(4):437–441, 1999.
- [5] Frank K Chen, Andre Luis de Castro Abreu, and Suzanne L Palmer. Utility of ultrasound in the diagnosis, treatment, and follow-up of prostate cancer: state of the art. *Journal of Nuclear Medicine*, 57(Supplement 3):13S–18S, 2016.
- [6] Gunjan Chugh, Shailender Kumar, and Nanhay Singh. Survey on machine learning and deep learning applications in breast cancer diagnosis. *Cognitive Computation*, 13(6):1451–1470, 2021.
- [7] Maarten De Rooij, Esther HJ Hamoen, Jurgen J Fütterer, Jelle O Barentsz, and Maroeska M Rovers. Accuracy of multiparametric mri for prostate cancer detection: a meta-analysis. *American Journal of Roentgenology*, 202(2):343–351, 2014.
- [8] Chengyuan Deng, Shihang Feng, Hanchen Wang, Xitong Zhang, Peng Jin, Yinan Feng, Qili Zeng, Yinpeng Chen, and Youzuo Lin. Openfwi: Large-scale multi-structural benchmark datasets for full waveform inversion. *Advances in Neural Information Processing Systems*, 35:6007–6020, 2022.
- [9] Shihang Feng, Hanchen Wang, Chengyuan Deng, Yinan Feng, Yanhua Liu, Min Zhu, Peng Jin, Yinpeng Chen, and Youzuo Lin.  $E^{FWI}$ : Multiparameter benchmark datasets for elastic full waveform inversion of geophysical properties. *Advances in Neural Information Processing Systems*, 36:23701–23713, 2023.
- [10] Kevin M Gilboy, Yixuan Wu, Bradford J Wood, Emad M Boctor, and Russell H Taylor. Dual-robotic ultrasound system for in vivo prostate tomography. In *Medical Ultrasound, and Preterm, Perinatal and Paediatric Image Analysis: First International Workshop, ASMUS 2020, and 5th International Workshop, PIPPI 2020, Held in Conjunction with MICCAI 2020, Lima, Peru, October 4-8, 2020, Proceedings 1*, pages 161–170. Springer, 2020.
- [11] Mohammad Havaei, Axel Davy, David Warde-Farley, Antoine Biard, Aaron Courville, Yoshua Bengio, Chris Pal, Pierre-Marc Jodoin, and Hugo Larochelle. Brain tumor segmentation with deep neural networks. *Medical image analysis*, 35:18–31, 2017.
- [12] National Cancer Institute. Cancer stat facts: Prostate cancer, 2024.
- [13] Veeru Kasivisvanathan, Antti S Rannikko, Marcelo Borghi, Valeria Panebianco, Lance A Mynderse, Markku H Vaarala, Alberto Briganti, Lars Budäus, Giles Hellawell, Richard G Hindley, et al. Mri-targeted or standard biopsy for prostate-cancer diagnosis. *New England Journal of Medicine*, 378(19):1767–1777, 2018.
- [14] Fu Li, Umberto Villa, Seonyeong Park, and Mark A Anastasio. 3-d stochastic numerical breast phantoms for enabling virtual imaging trials of ultrasound computed tomography. *IEEE transactions on ultrasonics, ferroelectrics, and frequency control*, 69(1):135–146, 2021.
- [15] Bilal Malik, Robin Terry, James Wiskin, and Mark Lenox. Quantitative transmission ultrasound tomography: Imaging and performance characteristics. *Medical physics*, 45(7):3063–3075, 2018.

- [16] Antun Maričić, Maksim Valenčić, Stanislav Sotošek, Romano Oguić, Aldo Ivančić, and Juraj Ahel. Transrectal sonography in prostate cancer detection—our 25 years experience of implementation. *Collegium antropologicum*, 34(2):239–242, 2010.
- [17] Tufve Nyholm, Stina Svensson, Sebastian Andersson, Joakim Jonsson, Maja Sohlin, Christian Gustafsson, Elisabeth Kjellén, Karin Söderström, Per Albertsson, Lennart Blomqvist, et al. Mr and ct data with multiobserver delineations of organs in the pelvic area—part of the gold atlas project. *Medical physics*, 45(3):1295–1300, 2018.
- [18] Sahil H Parikh, Charles Hesswani, William S Azar, Christopher R Koller, Kyle C Schuppe, Alexander P Kenigsberg, Neil Mendhiratta, Sarah Azari, Daniel Nethala, Yixuan Wu, et al. Mp30-01 a new look: The promising use of 3-dimensional quantitative transmission ultrasound tomography for the detection of prostate cancer an ex vivo study. *The Journal of Urology*, 211(5S):e490, 2024.
- [19] Jan Philipp Radtke and Boris Hadaschik. Re: Mri-targeted, systematic, and combined biopsy for prostate cancer diagnosis. *European Urology*, 78(2):291–292, 2020.
- [20] Nicole V Ruiter, Michael Zapf, Torsten Hopp, Hartmut Gemmeke, Koen WA van Dongen, Jorge Camacho, Joaquín L Herraiz, Maily Perez Liva, and Jose M Udías. Usct reference data base: Conclusions from the first spie usct data challenge and future directions. In *Medical Imaging 2018: Ultrasonic Imaging and Tomography*, volume 10580, pages 170–176. SPIE, 2018.
- [21] GY Sandhu, Cuiping Li, Olivier Roy, S Schmidt, and Neb Duric. Frequency domain ultrasound waveform tomography: breast imaging using a ring transducer. *Physics in Medicine & Biology*, 60(14):5381, 2015.
- [22] W Paul Segars, G Sturgeon, S Mendonca, Jason Grimes, and Benjamin MW Tsui. 4d xcat phantom for multimodality imaging research. *Medical physics*, 37(9):4902–4915, 2010.
- [23] Jeffrey J Tosoian, Yuping Zhang, Lanbo Xiao, Cassie Xie, Nathan L Samora, Yashar S Niknafs, Zoey Chopra, Javed Siddiqui, Heng Zheng, Grace Herron, et al. Development and validation of an 18-gene urine test for high-grade prostate cancer. *JAMA oncology*, 2024.
- [24] Bradley E Treeby and Benjamin T Cox. k-wave: Matlab toolbox for the simulation and reconstruction of photoacoustic wave fields. *Journal of biomedical optics*, 15(2):021314–021314, 2010.
- [25] Hanchen Wang, Yixuan Wu, Emad Bector, Songting Luo, and Youzuo Lin. Mask-enhanced deep-learning for prostate ultrasound tomography with narrow data acquisition aperture. In *Medical Imaging 2025: Ultrasonic Imaging and Tomography*, volume 13412, pages 175–181. SPIE, 2025.
- [26] Cheyenne Williams, Michael Daneshvar, Yixuan Wu, Jeunice Owens-Walton, Nitin Yerram, Patrick T Gomella, Luke P OConnor, Nabila Khondakar, Michael Ahdoot, Ayele Negussie, et al. Mp22-17 prostate ultrasound tomography (ut): correlation with mri and whole mount histopathology. *Journal of Urology*, 206(Supplement 3):e398, 2021.
- [27] James W Wiskin, Jacob Enders, Cheyenne Williams, Ismail Turkbey, Michael Rothberg, Michael Daneshvar, Maria Merino, Sheng Xu, Emad Bector, Yixuan Wu, et al. Imaging of prostate cancer with 3d ultrasound tomography. In *Medical Imaging 2022: Ultrasonic Imaging and Tomography*, page PC1203809. SPIE, 2022.
- [28] Yixuan Wu. *Multiparametric prostate ultrasound imaging*. PhD thesis, Johns Hopkins University, 2024.
- [29] Yixuan Wu, Jacob Enders, Cheyenne Williams, Baichuan Jiang, James Wiskin, Michael B Rothberg, Ayele H Negussie, John Klock, Lindsey Hazen, Sheng Xu, et al. Realistic digital phantoms for prostate ultrasound and photoacoustic imaging. In *Medical Imaging 2024: Ultrasonic Imaging and Tomography*, volume 12932, pages 318–327. SPIE, 2024.
- [30] Yue Wu and Youzuo Lin. InversionNet: An efficient and accurate data-driven full waveform inversion. *IEEE Transactions on Computational Imaging*, 6:419–433, 2019.

- [31] Zhijun Zeng, Youjia Zheng, Hao Hu, Zeyuan Dong, Yihang Zheng, Xinliang Liu, Jinzhuo Wang, Zuoqiang Shi, Linfeng Zhang, Yubing Li, and He Sun. Openwaves: A large-scale anatomically realistic ultrasound-CT dataset for benchmarking neural wave equation solvers, 2025.



Supplementary materials arrangement:

- Section A highlights the public resources to support the reproducibility and describes the licenses of the OPENPROS data and released code.
- Section B describes the detailed steps of how 2D phantoms are sliced from the 3D speed of sound volumes.
- Section C shows the naming strategy of the OPENPROS dataset.
- Section D describes the benchmark evaluation metrics of OPENPROS.
- Section E shows the baseline models' training configurations and hyper-parameters.
- Section F compares the widely used conventional k-Wave simulation method and our OPENPROS open-sourced simulation methods.

## A OPENPROS Public Resources and Licenses

First and foremost, the reproducibility of OPENPROS benchmarks is guaranteed by a number of public resources, listed below. Remarkably, we have a group (link available below) where any related discussion is welcome. Our team also promises to maintain the platform and support further developments based on the community feedback.

- **Website:** <https://open-pros.github.io>
- **Dataset URL:** <https://open-pros.github.io/datasets>
- **Github Benchmark Repository:** <https://github.com/hanchenwang/OpenPros>
- **Pretrained Models:**  
InversionNet checkpoint can be downloaded at: [https://drive.google.com/file/d/1TVrrzmVzUQvUyDTZ4il-EGH5EG60yFBL/view?usp=share\\_link](https://drive.google.com/file/d/1TVrrzmVzUQvUyDTZ4il-EGH5EG60yFBL/view?usp=share_link).  
ViT-Inversion checkpoint can be downloaded at: [https://drive.google.com/file/d/1TVrrzmVzUQvUyDTZ4il-EGH5EG60yFBL/view?usp=share\\_link](https://drive.google.com/file/d/1TVrrzmVzUQvUyDTZ4il-EGH5EG60yFBL/view?usp=share_link).
- **Google Group:** <https://groups.google.com/g/openfwi>

The codes are released on Github under **OSS** license and **BSD-3** license. We also attach the Creative Commons Attribution-NonCommercial-ShareAlike 4.0 International License to the data.

## B Details of 2D Phantom Extraction

Starting from our 3D prostate volumes (SOS maps and organ masks), we apply the following pipeline to produce each 2D phantom:

1. **Volume loading and isotropic resampling.** We load the segmentation masks and SOS volumes from each patient scan, resample anisotropic voxels onto a uniform 0.375 mm grid, and pad exterior regions with a baseline SOS of 1,500 m/s to emulate coupling gel.
2. **Initial probe placement.** A pair of valid points separated by 6 cm within the segmented rectum defines the transrectal transducer line. The abdominal transducer is then positioned 15 cm anterior along the same axis.
3. **Systematic rotation and translation.** To emulate clinical acquisition angles, we rotate both probe lines jointly from  $-45^\circ$  to  $+45^\circ$  in  $5^\circ$  increments and translate them within  $\pm 1$  mm in each Cartesian direction.
4. **Slice extraction.** At each probe configuration, we extract the 2D plane containing both transducer lines. The resulting slice preserves the true anatomical interfaces, tissue heterogeneity, and relative probe geometry.
5. **Random perturbations.** We add a small jitter of  $\pm 1^\circ$  to each rotation angle and  $\pm 1$  mm to each transducer coordinate to enrich variability.

Altogether, this procedure produces 280 000 unique 2D SOS phantoms with matching ultrasound data under limited-angle conditions. An illustration of the slicing geometry is shown in Figure 6.

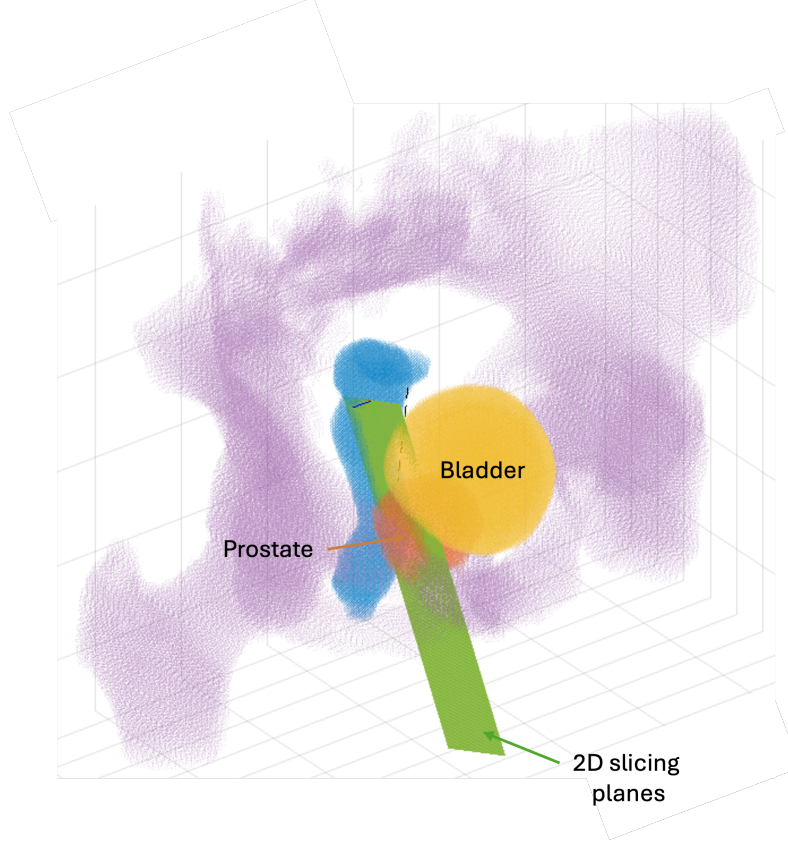


Figure 6: Schematic of our 2D phantom extraction. The green plane indicates the area between transrectal and abdominal probes.

### C Naming of OPENPROS

The data files follow a structured naming convention: `3_0{i}_P_{Date}_{Category}.npz`, where  $\{i\}$  represents patient IDs (1–4),  $\{Date\}$  denotes unique prostate sample identifiers, and  $\{Category\}$  specifies data types, including ultrasound data (`data`), segmentation labels (`mask`), and SOS maps (`sos`). For example, `3_02_P_2022-06-06_sos.npz` refers to SOS data for patient 3\_02 and prostate sample 2022-06-06.

### D Evaluation Metrics

To evaluate the performance of the proposed CNN-based reconstruction methods, we employ four quantitative metrics that comprehensively assess numerical accuracy and perceptual similarity between the reconstructed and true SOS images. Here, we denote the true SOS image as  $s$ , the predicted image as  $\hat{s}$ , and  $N$  as the total number of pixels in each image.

- **Mean Squared Error (MSE)** measures the pixel-wise squared differences:

$$\text{MSE} = \frac{1}{N} \sum_{i=1}^N (s_i - \hat{s}_i)^2, \quad (2)$$

where  $s_i$  and  $\hat{s}_i$  denote the true and predicted SOS values at pixel  $i$ .

- **Mean Absolute Error (MAE)** calculates the average absolute difference, providing robustness against outliers:

$$\text{MAE} = \frac{1}{N} \sum_{i=1}^N |s_i - \hat{s}_i|. \quad (3)$$

- **Structural Similarity Index Measure (SSIM)** assesses the perceptual quality, accounting for luminance, contrast, and structural similarities:

$$\text{SSIM}(s, \hat{s}) = \frac{(2\mu_s\mu_{\hat{s}} + C_1)(2\sigma_{s\hat{s}} + C_2)}{(\mu_s^2 + \mu_{\hat{s}}^2 + C_1)(\sigma_s^2 + \sigma_{\hat{s}}^2 + C_2)}, \quad (4)$$

where  $\mu_s, \mu_{\hat{s}}$  denote the means,  $\sigma_s, \sigma_{\hat{s}}$  the variances, and  $\sigma_{s\hat{s}}$  the covariance between true and predicted images. Constants  $C_1$  and  $C_2$  stabilize division by weak denominators.

- **Pearson Correlation Coefficient (PCC)** quantifies the linear correlation between true and predicted images, measuring structural consistency:

$$\text{PCC} = \frac{\sum_{i=1}^N (s_i - \bar{s})(\hat{s}_i - \bar{\hat{s}})}{\sqrt{\sum_{i=1}^N (s_i - \bar{s})^2} \sqrt{\sum_{i=1}^N (\hat{s}_i - \bar{\hat{s}})^2}}, \quad (5)$$

where  $\bar{s}$  and  $\bar{\hat{s}}$  denote the mean pixel values of the true and predicted SOS images, respectively.

## E Training Procedure

All baseline models (InversionNet and ViT-Inversion) were trained using a supervised learning approach on the proposed large-scale OPENPROS dataset. The dataset comprises a total of 280,080 samples, with 255,360 used for training and 27,360 for validation/testing.

For fair comparison, we kept the training settings identical across all methods. We employed the Adam optimizer with an initial learning rate of  $10^{-4}$ , a batch size of 512, and trained each model for up to 120 epochs. Early stopping was implemented based on validation set performance to prevent overfitting. Table 6 summarizes these training parameters.

Table 6: **Training parameters** consistently used across all baseline methods.

Total Epochs	Training Samples	Test Samples	Batch Size	Optimizer	Learning Rate
240	255,360	27,360	512	Adam	$10^{-4}$

The model sizes and training times for each baseline method are listed in Table 7. All experiments were conducted on NVIDIA H100 GPUs.

Table 7: **Computational cost and model size comparison** for baseline methods on the OPENPROS prostate USCT dataset.

Method	Training Cost (GPU hour)	Inference Cost (GPU second/sample)	Model Size
Beamforming	N/A	14400	N/A
USCT	N/A	86400	N/A
InversionNet	240	0.0049	20.45M
ViT-Inversion	128	0.0089	28.33M

## F Conventional k-Wave vs. Our Ultrasound Simulation Algorithms

Ultrasound imaging methods can be broadly categorized by their simulation paradigms. Conventional TRUS simulations, commonly used for B-mode imaging, rely on signal processing pipelines such as delay-and-sum (DAS) beamforming applied to simulated echoes. These simulations are often implemented using toolboxes like MATLAB k-Wave [24], which model acoustic wave propagation using pseudospectral methods and reconstruct images from envelope-detected signals. While fast and widely adopted in the clinical ultrasound community, this approach simplifies underlying physics and often introduces artifacts due to assumptions like homogeneous backgrounds, limited diffraction modeling, or approximate transducer responses.

In contrast, our dataset adopts a physically grounded modeling framework based on the 2D acoustic wave equation. We employ a finite-difference solver with fourth-order spatial and second-order temporal accuracy to simulate full-wave propagation through heterogeneous tissue. This method

captures wavefront curvature, multi-path scattering, and fine-grained variations in the SOS map, offering a far more realistic approximation of ultrasound interactions in complex anatomical regions such as the prostate. This fidelity is especially critical under limited-angle acquisition constraints common in prostate imaging, where traditional methods often fail to reconstruct accurate quantitative maps.

Unlike DAS-based methods, our simulation does not rely on beamforming post-processing, allowing it to serve as a foundation for quantitative imaging tasks like USCT. While k-Wave simulations are computationally efficient for B-mode image formation, our FDTD method remains tractable at scale and better suited for generating ground truth waveforms for learning-based inverse solvers.

Moreover, we provide two forward modeling solvers as part of our open-source release: a finite-difference solver with fourth-order spatial and second-order temporal accuracy, and an alternative Runge-Kutta implicit iterative solver. The former prioritizes accuracy and efficiency in time-domain modeling, while the latter offers enhanced numerical stability and can serve as a basis for future 3D extensions. Both solvers are publicly available with our dataset, supporting reproducibility and extensibility for ultrasound tomography and machine learning research. Additionally, the solvers support execution on both GPU and CPU platforms.